

# Precise Control of Quantum Confinement in Cesium Lead Halide Perovskite Quantum Dots via Thermodynamic Equilibrium

Yitong Dong,<sup>†</sup> Tian Qiao,<sup>†</sup> Doyun Kim,<sup>†</sup> David Parobek,<sup>†</sup> Daniel Rossi,<sup>†</sup> and Dong Hee Son\*,<sup>‡,§,ID</sup>

<sup>†</sup>Department of Chemistry, Texas A&M University, College Station, Texas 77843, United States

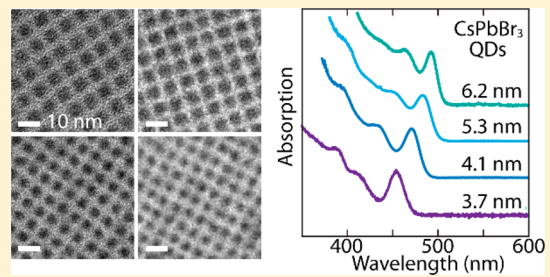
<sup>‡</sup>Center for Nanomedicine, Institute for Basic Science (IBS), Seoul 03722, Republic of Korea

## Supporting Information

**ABSTRACT:** Cesium lead halide ( $\text{CsPbX}_3$ ) nanocrystals have emerged as a new family of materials that can outperform the existing semiconductor nanocrystals due to their superb optical and charge-transport properties. However, the lack of a robust method for producing quantum dots with controlled size and high ensemble uniformity has been one of the major obstacles in exploring the useful properties of excitons in zero-dimensional nanostructures of  $\text{CsPbX}_3$ . Here, we report a new synthesis approach that enables the precise control of the size based on the equilibrium rather than kinetics, producing  $\text{CsPbX}_3$  quantum dots nearly free of heterogeneous broadening in their exciton luminescence.

The high level of size control and ensemble uniformity achieved here will open the door to harnessing the benefits of excitons in  $\text{CsPbX}_3$  quantum dots for photonic and energy-harvesting applications.

**KEYWORDS:** Perovskite, quantum dot, thermodynamic size control, ensemble uniformity



Cesium lead halide ( $\text{CsPbX}_3$ ) perovskite nanocrystals have attracted much attention as a superior alternative to many existing semiconductor nanocrystals in photonic<sup>1–6</sup> and photovoltaic<sup>7–9</sup> applications due to their excellent photo-physical properties such as high-photoluminescence quantum yields<sup>10–12</sup> and large carrier diffusion lengths.<sup>13</sup> In addition, highly labile halide ions in the lattice enable remarkably flexible modification of the nanocrystals' bandgap and structure via facile anion exchange.<sup>14–17</sup> However, the rapid growth rate in typical hot-injection synthesis conditions<sup>10</sup> usually produces nanocubes of  $>\sim 10$  nm in size, well outside of the quantum confinement regime, that exhibit bulk-like properties. Efforts have been made recently to reduce the size of  $\text{CsPbX}_3$  nanocubes to quantum confinement regime producing the quantum dots (QDs),<sup>10,18–22</sup> anticipating the similar benefits of confined exciton in well-developed II–VI and IV–VI QDs. For instance, the size of  $\text{CsPbBr}_3$  nanocubes could be reduced to  $\sim 4$  nm by varying the ligand composition (oleic acid-to-oleylamine ratio) or the amount of the oleylamine–HBr mixture in the reaction.<sup>21,22</sup> However, the controllability and uniformity of the QD size were still insufficient, with a limited ability to resolve the manifolds of size-dependent confined exciton transitions in the absorption spectra to the extent achieved in II–VI QDs. The challenge of producing  $\text{CsPbX}_3$  QDs with controlled size and high ensemble uniformity has been one of the major obstacles impeding the exploration and utilization of the properties of the strongly confined exciton in  $\text{CsPbX}_3$  QDs.<sup>6,19,23</sup>

Here, we report an unconventional yet highly effective method by which to tune the size of  $\text{CsPbX}_3$  QDs with very high ensemble uniformity based on thermodynamic equilibrium

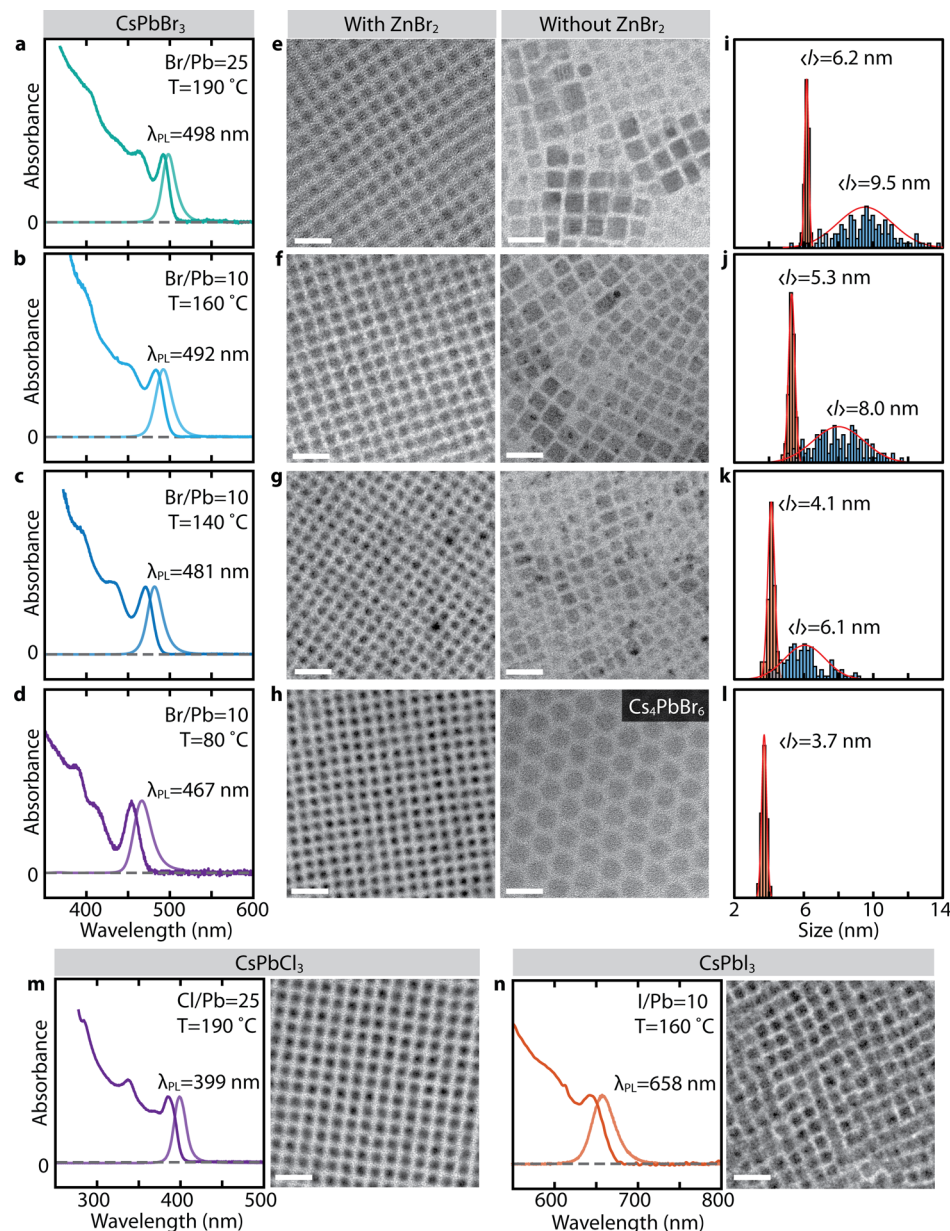
rather than the control of growth kinetics, a typical modality for the size control in most colloidal nanocrystal synthesis. We achieved the fine control of the QD size by exploiting the size-dependent stoichiometry of  $\text{X}^-$  in  $\text{CsPbX}_3$  QDs (higher  $\text{X}^-$  content in the smaller QDs) and the equilibrium of  $\text{X}^-$  between the QD and solution medium. While it is generally difficult to control the size of inorganic nanocrystals via thermodynamic equilibrium, we consider that the highly labile nature of  $\text{X}^-$  in  $\text{CsPbX}_3$  enables the utilization of the equilibrium for size control. This is extremely useful because the burden of controlling the nucleation and growth kinetics to obtain size control and uniformity in conventional nanocrystal synthesis<sup>24,25</sup> is relieved. While the present work focuses primarily on  $\text{CsPbBr}_3$ , the same synthesis approach applies to the synthesis of  $\text{CsPbX}_3$  QDs for  $\text{X} = \text{Cl}, \text{Br}$ , and  $\text{I}$ , indicating the universality of the thermodynamic equilibrium in  $\text{CsPbX}_3$  synthesis. Below, we demonstrate the capability of the new approach in controlling the size of  $\text{CsPbX}_3$  QDs in the quantum confinement regime with very high ensemble uniformity and present the evidence for the size control via thermodynamic equilibrium.

Figure 1a–d shows the absorption and PL spectra of  $\text{CsPbBr}_3$  QDs of several different sizes synthesized using varying combinations of  $\text{Br}^-$  concentration ( $[\text{Br}^-]$ ), parameterized as the Br-to-Pb ratio in the reactant for a fixed amount of  $\text{Cs}^+$  and  $\text{Pb}^{2+}$ , and the reaction temperature ( $T$ ). The corresponding representative transmission electron microscopy

Received: March 1, 2018

Revised: April 8, 2018

Published: May 4, 2018



**Figure 1.** Controlling the size of CsPbX<sub>3</sub> QDs with high ensemble uniformity. (a–d) Absorption and PL spectra of CsPbBr<sub>3</sub> QDs of different sizes. The reaction condition (Br-to-Pb ratio and temperature) and the PL peak wavelengths ( $\lambda_{PL}$ ) are indicated in each panel. The average size of the QDs,  $\langle l \rangle$ , is (a) 6.2 nm, (b) 5.3 nm, (c) 4.1 nm, and (d) 3.7 nm. (e–h, left panels) TEM images of the QDs corresponding to the optical spectra shown in panels a–d. (e–h, right panels) TEM images of CsPbBr<sub>3</sub> QDs synthesized using without ZnBr<sub>2</sub> as an excess source of Br<sup>-</sup> (i.e., Br/Pb = 2) at the same reaction temperatures as in the left panels. In the case of panel h, Cs<sub>4</sub>PbBr<sub>6</sub> was obtained instead of CsPbBr<sub>3</sub>. (i–l) Size distribution of CsPbBr<sub>3</sub> QDs produced using new (red) and previous (blue) methods shown in panels e–h. (m, n) Absorption and PL spectra and TEM images of CsPbCl<sub>3</sub> and CsPbI<sub>3</sub> QDs with  $\langle l \rangle$  values of 4.8 and 6.7 nm, respectively. All scale bars are 20 nm.

(TEM) images of the QDs are shown in the left panels of Figure 1e–h. The QD size is a function of the both Br-to-Pb ratio and the reaction temperature. At a fixed temperature, the QD size decreased with increasing Br-to-Pb ratio, simultaneously exhibiting the higher size uniformity with increasing Br-to-Pb ratios, as will be discussed further later. At a fixed Br-to-Pb ratio, the QD size decreased with decreasing temperature. By the choosing of the appropriate combination of these two parameters, precise tuning of the QD size in the quantum-confined regime was achieved with high ensemble uniformity. The QDs exhibit not only the well-defined band-edge exciton transition peak but also the peaks from the higher-energy exciton transitions previously not readily resolvable in the

absorption spectra.<sup>19–23</sup> (The assignment of peaks at the higher-energy region in the absorption spectra to the higher-energy exciton transitions was confirmed from the observation of the bleach in the pump–probe transient absorption spectra of these QDs. The result will be reported in future publications.) The photoluminescence (PL) is also narrower than the earlier reports (see Figure 2a) due to the high ensemble uniformity of the QD size. For CsPbBr<sub>3</sub>, very Br<sup>-</sup>-rich (Br/Pb = 10–25) conditions were required to obtain good size control below ~7 nm exhibiting strong quantum confinement. In this work, ZnBr<sub>2</sub> was used as the source of excess Br<sup>-</sup> with which to vary the Br-to-Pb ratio, such that Zn<sup>2+</sup> remains an inert bystander. In fact, other divalent-metal

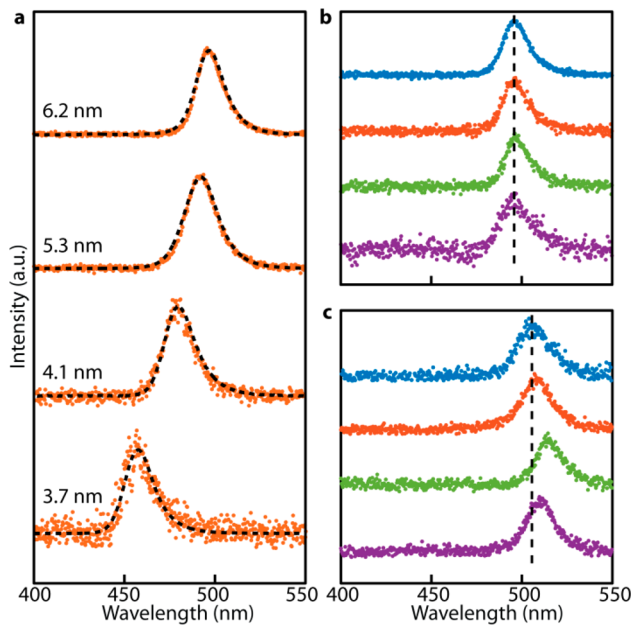


**Figure 2.** Single-particle PL spectra of  $\text{CsPbBr}_3$  QDs. (a) Comparison of the single-particle (dot) and ensemble (dashed line) PL spectra of  $\text{CsPbBr}_3$  QDs of different sizes. The full width at half-maximum (fwhm) of the ensemble PL is 94 meV for 6.2 nm, 109 meV for 5.3 nm, 117 meV for 4.1 nm, and 142 meV for 3.7 nm QDs. (b, c) Single-particle PL spectra of four randomly selected  $\text{CsPbBr}_3$  QDs in (b) monodisperse and (c) polydisperse QD ensemble compared in Figure 1e.

bromides (e.g.,  $\text{CoBr}_2$ ) can also provide the necessary  $\text{Br}^-$  and function similarly to  $\text{ZnBr}_2$  (Figure S1). Recently, the addition of HBr was also shown to have the effect of reducing the size, while the ensemble heterogeneity remained,<sup>21</sup> further corroborating the critical role of  $\text{Br}^-$ . To rule out the possibility of cations from  $\text{MBr}_2$  or organic ligands playing a critical role instead of  $\text{Br}^-$ , the lack of size controllability from zinc stearate and additional protonated ligands was also confirmed (Figure S1). It is important to mention that varying the concentration of  $\text{Cs}^+$  or  $\text{Pb}^{2+}$  in the reaction mixture formed either a Pb-deficient insulator phase or  $\text{CsPbBr}_3$  nanocrystals in a non-confinement regime exhibiting no size controllability.

In the TEM images of  $\text{CsPbBr}_3$  QDs (the left panels of Figure 1e–h), highly regular cubic arrangements of QDs were observed due to their uniform size and shape. Additional TEM images showing different areas and at different length scales (provided in Figure S2) showed superlattices formed by nanocubes, further demonstrating high size uniformity. An extensive survey of the TEM images found no sign of the other morphologies, such as nanoplatelets, previously seen in the earlier syntheses of  $\text{CsPbBr}_3$  nanocubes as the minor byproducts. These minor contaminants are also identifiable in the absorption spectrum as an additional exciton peak, e.g., near 430 or 460 nm<sup>10</sup> (Figure S3), if introduced deliberately. To highlight the exquisite size control gained in the new approach and the necessity of a high Br-to-Pb ratio, TEM images of the nanocrystals synthesized without  $\text{ZnBr}_2$  (i.e.,  $\text{Br}/\text{Pb} = 2$ ) at the same reaction temperatures are compared in the right panels of Figure 1e–h. The size distributions of the QDs from these two syntheses are compared in Figure 1i–l, which clearly shows the drastic change in the size uniformity in the ensemble. The comparison of absorption spectra of QDs in these two syntheses is also made in Figure S4. Figure 1m,n shows the

absorption, PL spectra, and TEM images of  $\text{CsPbCl}_3$  and  $\text{CsPbI}_3$  QDs of one chosen size produced by employing the same method as that described above. The additional absorption spectra of  $\text{CsPbCl}_3$  and  $\text{CsPbI}_3$  QDs of varying sizes in the quantum confinement regime are shown in Figure S5. The universal applicability of the same approach to three different halide perovskite QDs is another advantage of our method in comparison with other procedures. While the QDs of  $\text{CsPbCl}_3$  and  $\text{CsPbI}_3$  can also be obtained by the anion exchange of  $\text{CsPbBr}_3$  QDs (Figure S6), the direct synthesis is more convenient for producing the QDs in a large quantity without deterioration of the size uniformity.

The high ensemble uniformity of the size of  $\text{CsPbBr}_3$  QDs is further demonstrated in the comparison of the ensemble and single-particle PL at room temperature for four different sizes, which are nearly indistinguishable from each other as shown in Figure 2a. The full width at half-maximum (fwhm) line widths of the ensemble PL shown in Figure 2a are narrower (by 10–30%) than those from the earlier measurements made on the QDs of similar average size synthesized in different ways<sup>22</sup> or the QDs obtained via post-synthesis size selection.<sup>18</sup> Figure 2b,c shows multiple single-particle PL spectra of randomly chosen QDs belonging to the ensemble made with and without excess  $\text{Br}^-$ , respectively. Additional single-particle spectra of the QDs used for Figure 2b are provided in Figure S7. The spectra in Figure 2b are nearly identical to each other consistent with high ensemble uniformity, which is in contrast to those in Figure 2c, exhibiting the variation of the PL peak position. While the present single-particle PL data still has statistical probability of observing more than one QD, Figure 2c shows our measurement's ability to clearly distinguish the QDs of different sizes in a heterogeneous ensemble. Despite such a limit, the near-identical PL spectra in Figure 2b (and in Figure S7) corroborate a very high ensemble uniformity of the QDs that was previously unachievable.

X-ray diffraction (XRD) patterns of several different sized  $\text{CsPbBr}_3$  QDs show nearly the same patterns as the larger  $\text{CsPbBr}_3$  nanocrystals synthesized in the absence of  $\text{ZnBr}_2$  without noticeable peak shifts, while the peak broadens in the smaller QDs as expected (Figure S8). Elemental analysis from inductively coupled plasma–mass spectrometry and energy dispersive X-ray spectroscopy (EDS) indicated no sign of the incorporation of  $\text{Zn}^{2+}$  from  $\text{ZnBr}_2$  to the lattice beyond the detection limit of the measurement ( $\text{Zn}/\text{Pb} < 1 \times 10^{-3}$ ), setting an upper limit of  $<1 \text{ Zn}^{2+}$  ion per QD. A previous study using Zn salts in hot injection synthesis condition also reported no incorporation of  $\text{Zn}^{2+}$  in their samples,<sup>26</sup> although it can be introduced into the lattice via long ( $>10$  h) cation exchange process.<sup>27</sup> These indicate that, despite the presence of a large amount of  $\text{ZnBr}_2$  required to obtain good size control, the low probability of  $\text{Zn}^{2+}$  incorporation in  $\text{CsPbX}_3$  lattice under our hot-injection reaction conditions makes  $\text{ZnBr}_2$  a suitable source of extra  $\text{Br}^-$ . The PL quantum yield ( $\text{QY}_{\text{PL}}$ ) of  $\text{CsPbBr}_3$  QDs was 80–95% (Table 1) and has a PL lifetime in the range of 4–6 ns (Figure S9). These values are significantly higher than the  $\text{QY}_{\text{PL}}$  of  $\text{CsPbBr}_3$  QDs prepared by varying the acid and base composition of ligands (30–50%).<sup>22</sup> The absorption and PL spectra of these QDs in hexane solution stored in a vial contacting air at room temperature remained unchanged after 6 months, demonstrating their high colloidal stability at ambient conditions (Figure S10a). QDs made in this work are also stable under long UV excitation by both continuous-wave (10 h) and femtosecond pulsed lasers (6 h), which is important for

**Table 1. Stoichiometric Cs-to-Pb and Br-to-Pb Ratios and PL Quantum Yield ( $QY_{PL}$ ) of  $\text{CsPbBr}_3$  QDs<sup>a</sup>**

QD size	Cs-to-Pb ratio	Br-to-Pb ratio	$QY_{PL}$ (%)
9.5 nm	$0.77 \pm 0.01$	$2.6 \pm 0.1$	85–95
6.2 nm	$0.75 \pm 0.01$	$3.1 \pm 0.2$	85–95
5.3 nm	$0.75 \pm 0.01$	$3.2 \pm 0.2$	80–90
3.7 nm	$0.79 \pm 0.01$	$3.5 \pm 0.1$	80–90

<sup>a</sup>The Cs-to-Pb and Br-to-Pb ratios were obtained from ICP mass spectrometry and energy-dispersive X-ray spectroscopy (EDS), respectively.

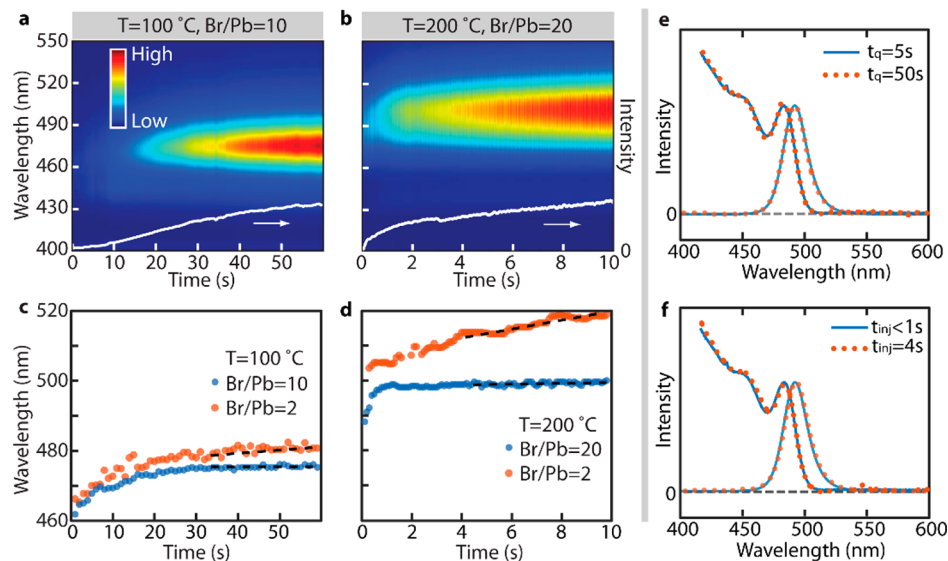
the reliable characterization of excitons in strongly confined QDs using both static and time-resolved spectroscopy. A comparison of the absorption spectra before and after the UV excitation, showing no noticeable spectral change, is provided in Figure S10b,c.

While fully understanding the size control mechanism requires further experimental and theoretical studies, the observations made here suggests the thermodynamic equilibrium of  $\text{Br}^-$  between the QD lattice and solution medium is the key factor determining the QD size. Evidence supporting this mechanism was obtained from the measurement of time-dependent PL under varying reaction conditions in conjunction with the negative correlation between the QD size and the Br-to-Pb ratio in the reaction mixture. Figure 3a,b show contour plots of the time-dependent PL spectra of  $\text{CsPbBr}_3$  QDs synthesized under two different reaction conditions, indicated in each panel. The curve superimposed on each contour plot shows the time dependence of the PL intensity ( $I_{PL}$ ) at the peak of the PL spectra ( $\lambda_{PL}$ ). Figure 3c,d shows the corresponding time-dependent  $\lambda_{PL}$  data compared with those from the reaction in the absence of excess  $\text{Br}^-$  (i.e., Br/Pb = 2). The red-shifting time-dependent PL spectra during the early times, not clearly discernible in the contour plots, are provided in Figure S11. A pair of important features observed in the

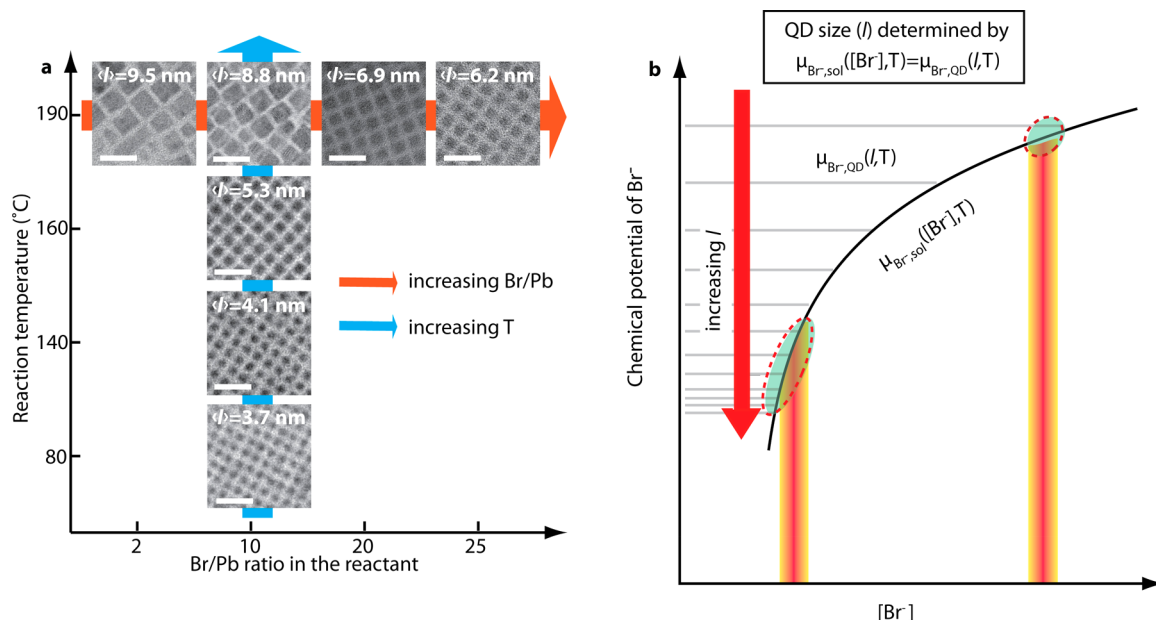
time-dependent PL from both QDs are two-fold. (1)  $\lambda_{PL}$  reaches the terminal value early during the reaction (~25 and ~1 s for panels a and c and panels b and d in Figure 3, respectively) and does not change further as the reaction continues when the  $\text{Br}^-$  equilibrium at high Br-to-Pb ratios is invoked to control the QD size. This is in clear contrast to the behavior of  $\lambda_{PL}$  at Br/Pb = 2 that continues to red-shift in the same time window. (2)  $I_{PL}$  in Figure 3a,b continues to increase long after the terminal  $\lambda_{PL}$  is reached until the reaction is quenched by rapid cooling. This indicates that the terminal size is independent of the long-time growth kinetics, while the extended reaction time increases the number of QDs for the same terminal size.

Figure 3e,f clearly shows the independence of the absorption and PL spectra of  $\text{CsPbBr}_3$  QDs on both the quenching time and the Cs precursor injection rate to the reactant mixture. Figure 3e compares the absorption and PL spectra of  $\text{CsPbBr}_3$  QDs with different quenching time ( $t_q$  = 5 and 50 s) with the swift ( $\ll 1$  s) injection of Cs precursor for the reaction at 160 °C and with Br/Pb = 10. The terminal  $\lambda_{PL}$  of 492 nm is reached at <5 s under this condition, and the optical spectra of the QDs are independent of the overall reaction time after 5 s. Figure 3f compares the absorption and PL spectra of  $\text{CsPbBr}_3$  QDs produced under the same reaction condition as in Figure 3e while using two different time periods, over which the same amount of Cs precursor was injected ( $t_{inj} \ll 1$  and 4 s). Both reactions were quenched at 50 s to recover the produced QDs. Despite the different nucleation kinetics anticipated by the different rates of addition for Cs precursor to the reaction mixture, the QDs exhibit the identical optical spectra indicating the same size. For this reason, the size and the optical spectra of the QDs are very reproducible in different batches of synthesis if the amount of reactants and reaction temperatures are kept the same.

A qualitative insight into the role of  $\text{Br}^-$  equilibrium in controlling the size of  $\text{CsPbBr}_3$  QDs can be obtained from the



**Figure 3.** Time-dependent PL spectra during the synthesis of  $\text{CsPbBr}_3$  QDs. (a, b) Contour plots of the time-dependent PL during the synthesis of  $\text{CsPbBr}_3$  QDs under two different reaction conditions: (a)  $T = 100$  °C, Br/Pb = 10 and (b)  $T = 200$  °C, Br/Pb = 20. (c, d) Comparison of the time-dependent  $\lambda_{PL}$  during the reaction shown in panel c at  $T = 100$  °C for Br/Pb = 10 and 2 and that shown in panel d at  $T = 200$  °C for Pb/Br = 20 and 2. (e, f) Comparison of the absorption and PL spectra of  $\text{CsPbBr}_3$  QDs synthesized using different (e) quenching time ( $t_q$ ) and (f) durations of Cs precursor injection ( $t_{inj}$ ). All of the reactions in panels e and f were performed at  $T = 160$  °C with Br/Pb = 10, producing the QDs with  $\lambda_{PL} = 492$  nm.



**Figure 4.** Size control via thermodynamic equilibrium in CsPbBr<sub>3</sub> QDs. (a) Dependence of the QD size on the Br-to-Pb ratio in the reactant and the reaction temperature. (b) A simple model illustrating the determination of the QD size via equilibrium of Br<sup>-</sup> between the QD lattice and solution medium. The QD size ( $l$ ) for a given Br<sup>-</sup> concentration ([Br<sup>-</sup>]) and temperature ( $T$ ) is determined where the chemical potentials of Br<sup>-</sup> in the QD ( $\mu_{\text{Br}^-, \text{QD}}$ , series of gray horizontal lines for different  $l$ ) and in the solution phase ( $\mu_{\text{Br}^-, \text{sol}}$ , black curve) become equal.

negative correlation between the QD size and [Br<sup>-</sup>] in the reactant mixture. An earlier study suggested that the outermost layer of the nanocrystal possess the composition of PbBr<sub>4</sub>,<sup>28</sup> which would result in a higher relative Br<sup>-</sup> content with decreasing size. The generally increasing stoichiometric Br-to-Pb ratio with decreasing QD size is confirmed by the elemental analysis as shown in Table 1. Because Br<sup>-</sup> is the most-labile species of CsPbBr<sub>3</sub> diffusing with a low kinetic barrier within the lattice, the QD size would be the most susceptible to the variation of Br<sup>-</sup> equilibrium between the QD and solution medium. The systematic decrease of the QD size with increasing [Br<sup>-</sup>], parametrized as the Br-to-Pb ratio in the reactant, at a given temperature is clearly seen in Figure 4a. The increasing size uniformity with increasing Br-to-Pb ratio is also apparent in the series of TEM images in Figure 4a. For a given Br-to-Pb ratio, the QD size increases with increasing temperature. The absorption spectra of CsPbBr<sub>3</sub> QDs corresponding to the variation of each parameter are given in Figure S12.

Here, we propose a simplified model based on the Br<sup>-</sup> equilibrium between the QD lattice and solution medium, consistent with the observed negative correlation between the QD size and the Br-to-Pb ratio (or [Br<sup>-</sup>]) and the higher size uniformity at the higher Br-to-Pb ratio (or [Br<sup>-</sup>]). In this model, the control of the QD size ( $l$ ) with the Br-to-Pb ratio can be viewed as satisfying the following equilibrium condition, as illustrated in Figure 4b:

$$\mu_{\text{Br}^-, \text{sol}}([Br^-], T) = \mu_{\text{Br}^-, \text{QD}}(l, T) \quad (1)$$

where  $\mu_{\text{Br}^-, \text{sol}}([Br^-], T)$  is the chemical potential of Br<sup>-</sup> at a given [Br<sup>-</sup>] and temperature  $T$  in the solution medium.  $\mu_{\text{Br}^-, \text{QD}}(l, T)$  is the chemical potential of Br<sup>-</sup> in the lattice of QD with size  $l$  at temperature  $T$ .  $\mu_{\text{Br}^-, \text{sol}}([Br^-], T)$  should increase approximately logarithmically with [Br<sup>-</sup>] following  $\mu_{\text{Br}^-, \text{sol}}([Br^-], T) = \mu_{\text{Br}^-, \text{sol}}^{\circ} + RT \ln(\gamma[Br^-])$ , where  $\mu_{\text{Br}^-, \text{sol}}^{\circ}$ ,  $R$ , and  $\gamma$  are the chemical potential at the standard state, gas constant, and activity coefficient, respectively. A series of

horizontal lines in Figure 4b represent  $\mu_{\text{Br}^-, \text{QD}}(l, T)$  for different values of  $l$  with the same increment of  $l$  ( $\Delta l$ ).  $\mu_{\text{Br}^-, \text{QD}}(l, T)$  is smaller for the larger  $l$  because the Br<sup>-</sup> composition in QD decreases with increasing  $l$  due to the Br<sup>-</sup>-rich surface relative to the interior.  $\mu_{\text{Br}^-, \text{QD}}(l, T)$  is also expected to show stronger dependence on  $l$  for smaller  $l$  due to the higher surface-to-volume ratio for smaller QDs. The larger spacing between the two adjacent lines representing  $\mu_{\text{Br}^-, \text{QD}}(l, T)$  for the smaller  $l$  represents the stronger dependence of  $\mu_{\text{Br}^-, \text{QD}}(l, T)$  on  $l$  for the smaller  $l$  in Figure 4b. The negative correlation between the QD size and [Br<sup>-</sup>] can be readily understood from the two circled areas in Figure 4b that indicate the regions of  $l$  satisfying the equilibrium condition expressed by eq 1 for the low- and high-[Br<sup>-</sup>] conditions at a given  $T$ . The higher uniformity of QD size obtained at the higher [Br<sup>-</sup>] can also be explained with this model. The range of  $l$  satisfying eq 1 for a small range of [Br<sup>-</sup>] represented by the width of vertical bar shown in orange in Figure 4b is smaller at the higher [Br<sup>-</sup>], indicating the narrower size distribution of the QDs synthesized at the higher [Br<sup>-</sup>] condition. The decreasing QD size with decreasing  $T$  for a given [Br<sup>-</sup>] could be phenomenologically described as the result of downward shift of the horizontal lines representing  $\mu_{\text{Br}^-, \text{QD}}(l, T)$  for different  $l$ , in addition to the variation of  $\mu_{\text{Br}^-, \text{sol}}([Br^-], T)$  with  $T$ . However, a more-complete and microscopic understanding of all aspects of the size control and uniformity will require a more-elaborate model, which is beyond the scope of this study.

Apparently, the equilibrium is operating at the reaction temperatures in this study (100–200 °C) determining the QD size. However, rapid cooling to room temperature seems to provide a sufficient energy barrier to keep the QDs stable without further change in size under ambient conditions and even under UV excitation for a reasonably long period, as discussed earlier. It is also worth pointing out that the relatively low structural stability of CsPbX<sub>3</sub> QDs in a harsh environment compared with other QDs such as CdSe, presumably due

partially to the high halide mobility, is dramatically improved by utilizing halide equilibrium. For instance, while  $\text{CsPbBr}_3$  QDs disintegrate when put into the heated solution (ODE at 140 °C), the addition of extra  $\text{Br}^-$  from  $\text{ZnBr}_2$  in the solution prevents the disintegration of the QDs (Figure S13). In contrast, the addition of zinc stearate did not prevent the dissolution of the QDs, indicating that it is  $\text{Br}^-$  and not  $\text{Zn}^{2+}$  that prevents the dissolution. This suggests that one could improve the stability of  $\text{CsPbX}_3$  QDs in their application by providing a surrounding environment rich in their respective halide.

**Conclusions.** We report a unique synthetic approach producing  $\text{CsPbX}_3$  QDs with precisely controlled size and high ensemble uniformity by utilizing the thermodynamic equilibrium instead of the kinetic control. The size of the QDs was controlled by varying only the Br-to-Pb ratio in the reactant and the reaction temperature while being completely insensitive to the nucleation and growth kinetics. QDs virtually free from the heterogeneous broadening in their room-temperature PL spectra were obtained in a broad spectral range thanks to the superb ensemble uniformity of the size. The ability to produce precisely size-controlled  $\text{CsPbX}_3$  QDs with near-perfect spectroscopic homogeneity will enable the understanding and practical application of the quantum-confined exciton in this new family of QDs. Furthermore, because the hybrid lead halide perovskites also possess labile halide ions,<sup>29–32</sup> we anticipate that the thermodynamic equilibrium of halide can also be utilized to obtain the QDs of hybrid perovskites with precise size control.

**Experimental Section. Material Synthesis.** The Cs-oleate precursor solution was prepared in a 50 mL three-necked round-bottomed flask by dissolving  $\text{Cs}_2\text{CO}_3$  (0.25 g) in a mixture of oleic acid (OA, 0.8 g) and 1-octadecene (ODE, 7 g) at 150 °C for >10 min under a  $\text{N}_2$  atmosphere on a Schlenk line. The temperature of the Cs-oleate solution was maintained above 100 °C to avoid precipitation. The precursor solution of Pb and X (halide; X = Cl or Br) was prepared by dissolving  $\text{PbX}_2$  (75 mg for  $\text{PbBr}_2$ ) and a varying amount of  $\text{ZnX}_2$  (0–600 mg) in a mixture of ODE (5 mL), OA (2 mL), and oleylamine (OAm, 2 mL) in a 25 mL three-necked round-bottomed flask under a  $\text{N}_2$  atmosphere at 120 °C for 10 min. For  $\text{CsPbI}_3$ , the precursor solution of Pb and I was prepared by dissolving  $\text{PbI}_2$  (120 mg) and  $\text{ZnI}_2$  (0–600 mg) in a mixture of trioctylphosphine (TOP, 5 mL), OA (1 mL), and OAm (1 mL) in a 25 mL three-necked round-bottomed flask under a  $\text{N}_2$  atmosphere.

After the setting of the temperature of the precursor solution of Pb and X at a chosen reaction temperature, 0.4 mL of Cs precursor solution was injected to initiate the reaction. The reaction was quenched after a short period of time (10–180 s, depending on the temperature in the range of 190–80 °C) by cooling the flask in an ice bath. The product was centrifuged at 3500 rpm to remove the unreacted salts as the precipitate, and the quantum dots (QDs) dispersed in the supernatant were collected. The thorough removal of unreacted salts is necessary to obtain pure QDs and avoid the formation of side products (e.g., nanowires or nanoplatelets) during the subsequent purification step. The QDs in the recovered supernatant solution were subsequently precipitated by adding ~8 mL of acetone. For  $\text{CsPbI}_3$  QDs, methyl acetate was used as the antisolvent. The precipitated QDs were used for further characterization after resuspending in hexane. In all of the syntheses, OA and OAm were vacuum-dried for 1 h at 120 °C

using a Schlenk line. Additional details of the synthesis are given in the Supporting Information.

**Characterization.** A fiberoptic-coupled CCD spectrometer (Ocean Optics, QE65pro) was used under the high-speed acquisition mode to collect time-dependent PL spectra. An optical fiber coupled with a collimating lens was placed close to the reaction flask collecting the PL from the top of the solution. The entire flask was illuminated with a UV lamp ( $\lambda = 375$  nm) from above the flask, while the reaction mixture was constantly stirred during the reaction.

The single-particle PL spectra of individual  $\text{CsPbBr}_3$  nanoparticle were obtained with a home-built wide-field microscope constructed with an image spectrograph (Princeton Instruments, Acton SpectraPro SP-2300) and an electron-multiplying charge-coupled device (EMCCD) (Princeton Instruments, ProEM 16002). For each QD sample, a highly diluted colloidal solution was drop-cast onto a thin quartz plate and placed on top of a quartz prism using index-matching oil to excite the QDs via attenuated total reflection (ATR). The sample was excited at 405 nm with a 10 nm bandwidth using a Xe lamp (Oriel Instrument, 300 W) in conjunction with a monochromator (Newport, Oriel Cornerstone 130). The PL from a well-separated single  $\text{CsPbBr}_3$  QD collected with the objective (Olympus, PLanFL N 40 $\times$ ) was projected on the narrow slit of the imaging spectrograph using a tube lens (Nikon) and sent to the EMCCD either as an image or as a dispersed spectrum. Details regarding the instrument used for this measurement are given elsewhere.<sup>33</sup>

TEM images were obtained on a FEI Tecnai G2 F20 ST field-emission TEM microscope at 200 kV. Powder X-ray diffraction data were collected using a Bruker-AXS Venture IuS CMOS  $\kappa$  X-ray diffractometer equipped with Cu IuS microfocus X-ray radiation and a kappa D8 goniometer. Elemental analysis was performed using inductively coupled plasma mass spectrometry (Nexlon 300D) and the TEM described previously (equipped for EDS) to determine the amount of metal cations and halogen anions in all of the samples. Due to the difficulty in thoroughly removing all unreacted metal salts, additional cleaning via gel permeation chromatography was used to ensure accurate analysis.<sup>34</sup> Briefly, 4 g of poly(styrene-divinylbenzene) gel was soaked in toluene overnight and then packed into a column with toluene as the mobile phase. QD samples could also be cleaned by precipitating them with ethyl acetate. The cleaned QDs were confirmed to show the same optical spectra before and after additional cleaning.

## ■ ASSOCIATED CONTENT

### S Supporting Information

The Supporting Information is available free of charge on the ACS Publications website at DOI: [10.1021/acs.nanolett.8b00861](https://doi.org/10.1021/acs.nanolett.8b00861).

Details on materials and additional experimental methods. Figures showing a comparison of the effects on size control, additional TEM images and optical spectra, XRD patterns, QD PL lifetimes and stability, time-resolved luminescence spectra, additional absorption spectra, and a comparison of the effects on high-temperature stability. ([PDF](#))

**AUTHOR INFORMATION****Corresponding Author**\*E-mail: [dhson@chem.tamu.edu](mailto:dhson@chem.tamu.edu).**ORCID**Dong Hee Son: [0000-0001-9002-5188](https://orcid.org/0000-0001-9002-5188)**Notes**

The authors declare no competing financial interest.

**ACKNOWLEDGMENTS**

This research was supported by the Robert A. Welch Foundation A-1639 (Y.D.), NSF DMR-1404457 (D.R.), NSF GRFP DGE-1252521 (D.P.), and IBS-R026-D1 (D.H.S.). Dr. Nattamai S. P. Bhuvanesh is acknowledged for assisting with XRD measurements.

**REFERENCES**

- (1) Song, J. Z.; Li, J. H.; Li, X. M.; Xu, L. M.; Dong, Y. H.; Zeng, H. B. *Adv. Mater.* **2015**, *27*, 7162–7167.
- (2) Yakunin, S.; Protesescu, L.; Krieg, F.; Bodnarchuk, M. I.; Nedelcu, G.; Humer, M.; De Luca, G.; Fiebig, M.; Heiss, W.; Kovalenko, M. V. *Nat. Commun.* **2015**, *6*, 8056.
- (3) Wang, Y.; Li, X. M.; Song, J. Z.; Xiao, L.; Zeng, H. B.; Sun, H. D. *Adv. Mater.* **2015**, *27*, 7101–7108.
- (4) Ramasamy, P.; Lim, D. H.; Kim, B.; Lee, S. H.; Lee, M. S.; Lee, J. S. *Chem. Commun.* **2016**, *52*, 2067–2070.
- (5) Kovalenko, M. V.; Protesescu, L.; Bodnarchuk, M. I. *Science* **2017**, *358*, 745–750.
- (6) Polavarapu, L.; Nickel, B.; Feldmann, J.; Urban, A. S. *Adv. Energy Mater.* **2017**, *7*, 1700267.
- (7) Swarnkar, A.; Marshall, A. R.; Sanehira, E. M.; Chernomordik, B. D.; Moore, D. T.; Christians, J. A.; Chakrabarti, T.; Luther, J. M. *Science* **2016**, *354*, 92–95.
- (8) Beal, R. E.; Slotcavage, D. J.; Leijtens, T.; Bowring, A. R.; Belisle, R. A.; Nguyen, W. H.; Burkhard, G. F.; Hoke, E. T.; McGehee, M. D. J. *Phys. Chem. Lett.* **2016**, *7*, 746–751.
- (9) Akkerman, Q. A.; Gandini, M.; Di Stasio, F.; Rastogi, P.; Palazon, F.; Bertoni, G.; Ball, J. M.; Prato, M.; Petrozza, A.; Manna, L. *Nat. Energy* **2016**, *2*, 16194.
- (10) Protesescu, L.; Yakunin, S.; Bodnarchuk, M. I.; Krieg, F.; Caputo, R.; Hendon, C. H.; Yang, R. X.; Walsh, A.; Kovalenko, M. V. *Nano Lett.* **2015**, *15*, 3692–3696.
- (11) Koscher, B. A.; Swabeck, J. K.; Bronstein, N. D.; Alivisatos, A. P. *J. Am. Chem. Soc.* **2017**, *139*, 6566–6569.
- (12) Liu, F.; Zhang, Y.; Ding, C.; Kobayashi, S.; Izuishi, T.; Nakazawa, N.; Toyoda, T.; Ohta, T.; Hayase, S.; Minemoto, T.; Yoshino, K.; Dai, S.; Shen, Q. *ACS Nano* **2017**, *11*, 10373–10383.
- (13) Yettagupu, G. R.; Talukdar, D.; Sarkar, S.; Swarnkar, A.; Nag, A.; Ghosh, P.; Mandal, P. *Nano Lett.* **2016**, *16*, 4838–4848.
- (14) Akkerman, Q. A.; D’Innocenzo, V.; Accornero, S.; Scarpellini, A.; Petrozza, A.; Prato, M.; Manna, L. *J. Am. Chem. Soc.* **2015**, *137*, 10276–10281.
- (15) Zhang, D. D.; Yang, Y. M.; Bekenstein, Y.; Yu, Y.; Gibson, N. A.; Wong, A. B.; Eaton, S. W.; Kornienko, N.; Kong, Q.; Lai, M. L.; Alivisatos, A. P.; Leone, S. R.; Yang, P. D. *J. Am. Chem. Soc.* **2016**, *138*, 7236–7239.
- (16) Parobek, D.; Dong, Y.; Qiao, T.; Rossi, D.; Son, D. H. *J. Am. Chem. Soc.* **2017**, *139*, 4358–4361.
- (17) Nedelcu, G.; Protesescu, L.; Yakunin, S.; Bodnarchuk, M. I.; Grotevent, M. J.; Kovalenko, M. V. *Nano Lett.* **2015**, *15*, 5635–5640.
- (18) Brennan, M. C.; Herr, J. E.; Nguyen-Beck, T. S.; Zinna, J.; Draguta, S.; Rouvimov, S.; Parkhill, J.; Kuno, M. *J. Am. Chem. Soc.* **2017**, *139*, 12201–12208.
- (19) Chen, J.; Žídek, K.; Chábera, P.; Liu, D.; Cheng, P.; Nuuttila, L.; Al-Marri, M. J.; Lehtivuori, H.; Messing, M. E.; Han, K.; Zheng, K.; Pullerits, T. *J. Phys. Chem. Lett.* **2017**, *8*, 2316–2321.
- (20) Sun, S. B.; Yuan, D.; Xu, Y.; Wang, A. F.; Deng, Z. T. *ACS Nano* **2016**, *10*, 3648–3657.
- (21) Dutta, A.; Dutta, S. K.; Das Adhikari, S.; Pradhan, N. *ACS Energy Lett.* **2018**, *3*, 329–334.
- (22) Almeida, G.; Goldoni, L.; Akkerman, Q.; Dang, Z.; Khan, A. H.; Marras, S.; Moreels, I.; Manna, L. *ACS Nano* **2018**, *12*, 1704–1711.
- (23) Butkus, J.; Vashishtha, P.; Chen, K.; Gallaher, J. K.; Prasad, S. K. K.; Metin, D. Z.; Laufersky, G.; Gaston, N.; Halpert, J. E.; Hodgkiss, J. M. *Chem. Mater.* **2017**, *29*, 3644–3652.
- (24) Park, J.; Joo, J.; Kwon, S. G.; Jang, Y.; Hyeon, T. *Angew. Chem., Int. Ed.* **2007**, *46*, 4630–4660.
- (25) Hendricks, M. P.; Campos, M. P.; Cleveland, G. T.; Jen-La Plante, L.; Owen, J. S. *Science* **2015**, *348*, 1226–1230.
- (26) Woo, J. Y.; Kim, Y.; Bae, J.; Kim, T. G.; Kim, J. W.; Lee, D. C.; Jeong, S. *Chem. Mater.* **2017**, *29*, 7088–7092.
- (27) van der Stam, W.; Geuchies, J. J.; Altantzis, T.; van den Bos, K. H. W.; Meeldijk, J. D.; Van Aert, S.; Bals, S.; Vanmaekelbergh, D.; de Mello Donega, C. *J. Am. Chem. Soc.* **2017**, *139*, 4087–4097.
- (28) Weidman, M. C.; Seitz, M.; Stranks, S. D.; Tisdale, W. A. *ACS Nano* **2016**, *10*, 7830–7839.
- (29) Pellet, N.; Teuscher, J.; Maier, J.; Grätzel, M. *Chem. Mater.* **2015**, *27*, 2181–2188.
- (30) Jang, D. M.; Park, K.; Kim, D. H.; Park, J.; Shojaei, F.; Kang, H. S.; Ahn, J.-P.; Lee, J. W.; Song, J. K. *Nano Lett.* **2015**, *15*, 5191–5199.
- (31) Lignos, I.; Protesescu, L.; Emiroglu, D. B.; Maceiczyk, R.; Schneider, S.; Kovalenko, M. V.; deMello, A. *Nano Lett.* **2018**, *18*, 1246–1252.
- (32) Protesescu, L.; Yakunin, S.; Kumar, S.; Bär, J.; Bertolotti, F.; Masciocchi, N.; Guagliardi, A.; Grotevent, M.; Shorubalko, I.; Bodnarchuk, M. I.; Shih, C.-J.; Kovalenko, M. V. *ACS Nano* **2017**, *11*, 3119–3134.
- (33) Jin, H.; Ahn, M.; Jeong, S.; Han, J. H.; Yoo, D.; Son, D. H.; Cheon, J. *J. Am. Chem. Soc.* **2016**, *138*, 13253–13259.
- (34) Shen, Y.; Gee, M. Y.; Tan, R.; Pellechia, P. J.; Greytak, A. B. *Chem. Mater.* **2013**, *25*, 2838–2848.